

On Curvature Estimation of ISO Surfaces in 3D Gray-Value Images and the Computation of Shape Descriptors

Bernd Rieger, Frederik J. Timmermans,
Lucas J. van Vliet, *Member, IEEE*, and
Piet W. Verbeek

Abstract—In this paper, we present a novel method to estimate curvature of iso gray-level surfaces in gray-value images. Our method succeeds where standard isophote curvature estimation methods fail. There is neither a segmentation of the surface needed nor a parametric model assumed. Our estimator works on the orientation field of the surface. This orientation field and a description of local structure is obtained by the Gradient Structure Tensor. The estimated orientation field has discontinuities mod π . It is mapped via the Knutsson mapping to a continuous representation. The principal curvatures of the surface, a coordinate invariant property, are computed in this mapped representation. From these curvatures, locally the bending energy is computed to describe the surface shape. An extensive evaluation shows that our curvature estimation is robust even in the presence of noise, independent of the scale of the object and furthermore the relative error stays small.

Index Terms—Principal curvatures, surface area, local surface measures, gradient structure tensor, Knutsson mapping.

1 INTRODUCTION

CURVATURES of surfaces are the key to compute shape descriptors and to classify different classes of surfaces. We have developed a novel method to estimate principal curvatures of iso surfaces that are implicitly represented by gray-level isophotes (level-sets). Surfaces are embedded in the image by a gray-level difference with respect to their surroundings. Our method works directly on the gray-value information of the image. Neither a segmentation is needed to detect the iso-level of the surface nor a parametric fit is done at any time during the analysis. The method exploits the differential structure of images.

The iso surface or isophote curvature $\frac{I_{TT}}{|\nabla I|}$ can successfully be applied to edges in 3D gray-value images [1], [2], [3], [4], [5], [6], but it fails when applied to curved plates, hollow objects, and concentric shells [7]. This is due to the fact that, on ridges and in valleys, the gradient magnitude $|\nabla I|$ is (nearly) zero. In Figs. 2c, 2d, 2e, and 2f, we show a shell of a 3D torus with a Gaussian ridge profile and computations of the mean curvature by our proposed algorithm and by the isophote curvature [4]. The numerator of the mean curvature by isophote curvature in Fig. 2e is smooth, but for all pixel on the ridge the normalization of the isophote curvature fails due to a vanishing gradient magnitude, resulting in a severe overestimation. These pixels are displayed white in Fig. 2f. The curvature computed by our proposed method does not suffer this problem.

Our algorithm can robustly estimate curvature of any 3D pattern hampered by noise. It is particularly useful for (concentric) shell patterns where isophote curvature also fails, compare Figs. 3d, 3e, and 3f. The regularization of the isophote curvature does not only reduce noise, but also suppresses such pseudoperiodic patterns at

- The authors are with the Pattern Recognition Group, Department of Applied Physics, Delft University of Technology, Lorentzweg 1, 2628 CJ Delft, The Netherlands. E-mail: {bernd, lucas, piet}@ph.tn.tudelft.nl.

Manuscript received 11 Feb. 2002; revised 20 Feb. 2003; accepted 11 Oct. 2003.

Recommended for acceptance by S. Dickinson.

For information on obtaining reprints of this article, please send e-mail to: tpami@computer.org, and reference IEEECS Log Number 115876.

the same time. The aforementioned problem can be overcome if we transform the gray-value image into an orientation map mod π (normal vector field up to sign) from which the curvatures are derived after solving the discontinuity problem. In 2D, the double angle method is well-known for solving the discontinuity in representing orientation [8], but in 3D, this problem remained an obstacle that prevented the computation of curvature. We solve this problem by mapping the orientation field via a quadratic form, the Knutsson mapping [9], [10], which is suitable for further processing and enables us to compute the curvatures.

In images that contain planar structures, the local bending energy, $\kappa_1^2 + \kappa_2^2$ [2], is a useful characteristic (local deformation energy) and can be computed per point with subpixel precision. It can be integrated over the object surface

$$E_B = \int \kappa_1^2 + \kappa_2^2 dA \quad (1)$$

into a scale invariant shape descriptor. A sphere minimizes bending energy for a given closed surface. Therefore, it can be seen as the roughness of a surface and can be used to characterize (biological) objects [11], [12]. Another shape descriptor is the Euler characteristic $\chi = \frac{1}{2\pi} \int \kappa_1 \kappa_2 dA$, which describes the global topology of a closed surface by an integer number. As a function of scale, χ is closely related to the morphological granulometry [13], [14], [15]. The latter is a volume weighted distribution, whereas χ counts the number of objects minus the number of handles (or tunnels) visible at a certain scale.

2 CURVATURES OF GRAY-VALUE SURFACES: THEORY AND ALGORITHMS

The curvature κ at a point p in a tangent direction T on a surface is defined as the magnitude of the change of the surface normal N (see, for example, [16], [17])

$$\kappa_T(p) = \|\nabla_T N\|. \quad (2)$$

There exist two mutual orthogonal tangent directions T_1 and T_2 , for which the curvatures are extremal. They are called principal directions, which associated curvatures κ_1 and κ_2 . Two classical measures of curvature in a point are the Gaussian $K := \kappa_1 \kappa_2$ and mean curvature $H := \frac{\kappa_1 + \kappa_2}{2}$. The shape index $s = \frac{2}{\pi} \arctan \frac{\kappa_2 + \kappa_1}{\kappa_2 - \kappa_1}$ [18] gives a qualitative classification of 2D surfaces by only one number.

2.1 Curvature Estimation Algorithm

In order to compute the principal curvatures and shape descriptors of iso surfaces embedded in gray-level images we need 1) to find the vector field normal N and the principal directions T_1 and T_2 and 2) solve the discontinuity problem of N and compute $\|\nabla_T N\|$.

2.1.1 Normal Field and Principal Directions by the Gradient Structure Tensor

The gradient structure tensor (GST) is a generic tool to analyze local structure in images [19], [20], [21], [22], [7], [23]. It is defined as $\bar{G} := \overline{\nabla \nabla^T}$ with $\nabla = \nabla I$, I is a gray-value image and the overhead bar $(\bar{\cdot})$ stands for averaging the elements over a local (Gaussian) neighborhood. The GST obtains its descriptive power from an analogy to a well-known quantity in physics, the inertia tensor $J_{ij} = \text{tr}(G_{ij})\delta_{ij} - G_{ij}$.

Two scales are involved. The gradient vector ∇I is computed by convolutions with Gaussian derivatives at the scale σ_g . The size of the Gaussian weighted tensor smoothing σ_T defines the neighborhood in which the image structure is computed. The latter can be used for noise suppression without hampering the signal strength. The tensor smoothing is usually chosen $2\sigma_g \leq \sigma_T \leq 10\sigma_g$. An

eigenvalue analysis of \bar{G} is a standard approach to classify local structure in images. In the case of planar structures, the eigenvalues will have the following ordering: $\lambda_1 \gg \lambda_2 > \lambda_3$. The eigenvector v_1 (corresponding to the largest eigenvalue λ_1) is aligned with the surface normal. The remaining two eigenvectors v_2, v_3 , lie in the principal directions of the surface. Summarizing, we find:

$$v_1 \leftrightarrow N, v_{2,3} \leftrightarrow T_{1,2}. \quad (3)$$

For cylindrical surfaces and at umbilic points on surfaces (e.g., spheres and planes), the true normal is a symmetry axis for all sizes of the local neighborhood σ_T . All symmetry axes, including the normal, coincide with the eigenvectors of the GST as is the case with the inertia tensor. Note also that the eigenvectors of the GST yield the “best” orientation estimate in a least-squares sense [24].

A drawback of the GST that the $\{v_i\}$ only contain orientation information $v_1 = \pm N$, (a discontinuous representation) is solved below.

2.1.2 Solving the Discontinuity Problem in Estimating of the Principal Curvatures

Now, we want to compute the principal curvatures by differentiating the normal with respect to the principal directions. From (2) and (3), we obtain

$$|\kappa_{1,2}| = \|\nabla_{T_{1,2}} N\| \leftrightarrow \|\nabla_{v_{2,3}} v_1\|. \quad (4)$$

Unfortunately, the calculated orientation field v_1 contains a discontinuity. Computation of partial derivatives of an orientation field are not possible without some preparation. A comprehensive review of this problem is given in [9], [10]. The idea is to transform v_1 into a continuous representation by a mapping M for which $\|\delta M(v)\| = K\|\delta v\|$ holds. A suitable mapping was introduced by Knutsson $M(v) = \frac{v v^T}{\|v\|}$, with $K = \sqrt{2}$ for $\|v\| = \text{const.}$ [8]. The norm of the mapped derivative $M(v)$ is linearly related to the norm of the derivative of v . Therefore, we propose a new expression, together with (3), that is suitable to compute curvature of surfaces in images

$$|\kappa_{1,2}| = \frac{1}{\sqrt{2}} \|\nabla_{v_{2,3}} M(v_1)\|. \quad (5)$$

Let the elements of $M(v_1) = \frac{v_1 v_1^T}{\|v_1\|}$ be M_{ij} and x^i a coordinate then (5) reads in explicit index notation

$$|\kappa_{1,2}| = \frac{1}{\sqrt{2}} \left\| \sum_{k=1}^3 \frac{\partial M_{ij}}{\partial x^k} v_{2,3}^k \right\|,$$

where the norm of M is defined as the Fröbenius norm $\|M\|^2 := \sum_{i,j} M_{ij}^2$. See Appendix B for a formal proof that (5) equals (2). The application of (5) to hypersurfaces in n dimensions is straightforward. The sign of the curvature, i.e., if we deal with an elliptic or hyperbolic Situation, is lost by the outlined algorithm. The sign can be retrieved, even for planar structures, as described in Appendix A.

2.2 From Surface Area Estimation to Shape Descriptors

In order to build (local) shape descriptors for objects based on these curvatures, we must be able to integrate the curvatures over the whole object surface, compare (1). To do this, we introduce a sampling-error free surface area estimator based on the sum of the samples in a local image. The local image is transformed into an image whose sum is proportional to the surface of the embedded object. With this technique at hand, we can now estimate globally the bending energy.

Assume a band-limited solid object is embedded in an image I by an iso surface at level ℓ . The surface area of the object $\int_S dA$ can be computed by a volume integral $\int_I \Phi[I(x)] dV$ after a

suitable transformation of the image. Here, we will focus on the main idea, for a more comprehensive discussion see [25], [26]. The transformation Φ must produce an image whose integrated volume = $\text{const.} \times$ surface area. Thus, each cross section $e(r)$ perpendicular to the iso surface S should contribute an equal amount. First, we apply erf-clipping (a form of soft-clipping) to the image between the limits $\ell \pm \frac{1}{2}h$. The cross section is a clipped edge, $e(r) = h - \int_0^r p(\tilde{r}) d\tilde{r}$ with profile distribution $p(\tilde{r})$ satisfying $\int_0^\infty p(\tilde{r}) d\tilde{r} = h$. Along the iso surface $\|\nabla I_{\text{clip}}\| = \|\frac{d}{dr} I_{\text{clip}}\|$. Note that the integral $\int \|\frac{d}{dr} I_{\text{clip}}\| dr = \int \|\frac{d}{dr} e(r)\| dr = h$. Finally, volume integration of $\|\nabla I_{\text{clip}}\|$ accumulates the contribution of all cross sections and, hence, $\frac{1}{h} \int \|\nabla I_{\text{clip}}\| dV$ yields the surface area of the embedded object. Thus, integration over an iso-surface element dA is accomplished by integration of the gradient magnitude after clipping over the entire image volume

$$\int_S dA = \frac{1}{h} \int_V \|\nabla I_{\text{clip}}\| dV. \quad (6)$$

The volume integral can be replaced by a sum of the sampled image iff $\|\nabla I_{\text{clip}}\|$ is approximately band-limited and sampled at half the Nyquist rate [1], [25]. Since $\|\nabla I\| \geq 0$, noise contributions will not compensate each other, but sum up over the entire image. A mask image can be used to only integrate over a region of interest. The mask can be computed from the gradient magnitude with a larger filter and then performing an iso-data threshold operation. Another possibility is to apply a nonlinear smoothing operation (e.g., anisotropic diffusion along the contour $\frac{dI}{dt} = -I_{TT}$ [27]) for preprocessing followed by an erf-clipping operation [25]. The sampling-error free measurement of the surface area is only possible if the object is solid. Filling shells can be done by a procedure described in Appendix A.

3 EVALUATION OF THE ALGORITHM

3.1 Test Images

We created band-limited gray-value test images containing shells of constant thickness of spheres and ellipsoids, see Fig. 3a and 3b. A band-limited ellipsoid shell is produced by computing the squared gradient magnitude of a band-limited filled ellipsoid. Isophote curvature estimation $\frac{I_{TT}}{\|I_T\|}$ applied to these images will fail as the gradient vanishes on ridges and valleys. The relative edge localization error of the gradient in 3D is about $-(\sigma/R)^2$ for constant curvature [26], where R is the bending radius and σ the standard deviation of the derivative filter. Therefore, the peak position of $\|\nabla I\|^2$ will be shifted, but this is neglectable for $R > 10$. We must satisfy $\sigma \geq 0.9\sqrt{2} \approx 1.3$ to ensure band-limitation [26].

3.2 Curvature

In this section, we investigate the performance of (5) on different ellipsoids with different levels of added Gaussian noise. An ellipsoid with half axes a, b, c (Fig. 1a) is given by the parametrization $(a \cos u \sin v, b \sin u \sin v, c \cos v)$, $u \in [0, 2\pi], v \in [0, \pi]$. Due to symmetry, it is sufficient to evaluate the algorithm in the first quadrant ($u \in [0, \pi/2]$) of the xy -plane ($v = \pi/2$). The first principal direction lies perpendicular to the xy -plane, whereas the second lies in it. The curvatures are computed for the whole image (via (5)) and then evaluated at the mathematical surface position. We can retrieve the values with subpixel precision as our test image is sampled correctly. In Fig. 1b, the estimated and true principal curvatures are plotted for three different ellipsoids with half axes $a = c$ and $b/a = 1.5$. The estimation is averaged over 20 subpixels shifts. The relative estimation error is about 1 percent at the blunt side ($u = 0, v = \pi/2$) and increases with increasing curvature to about 7 percent for $\kappa = 0.075$ at $u = \pi/2$. For curvatures smaller than 0.04, our estimation has very little bias ($\epsilon < 2$ percent). The small underestimation of the true curvature as observed in Fig. 1b

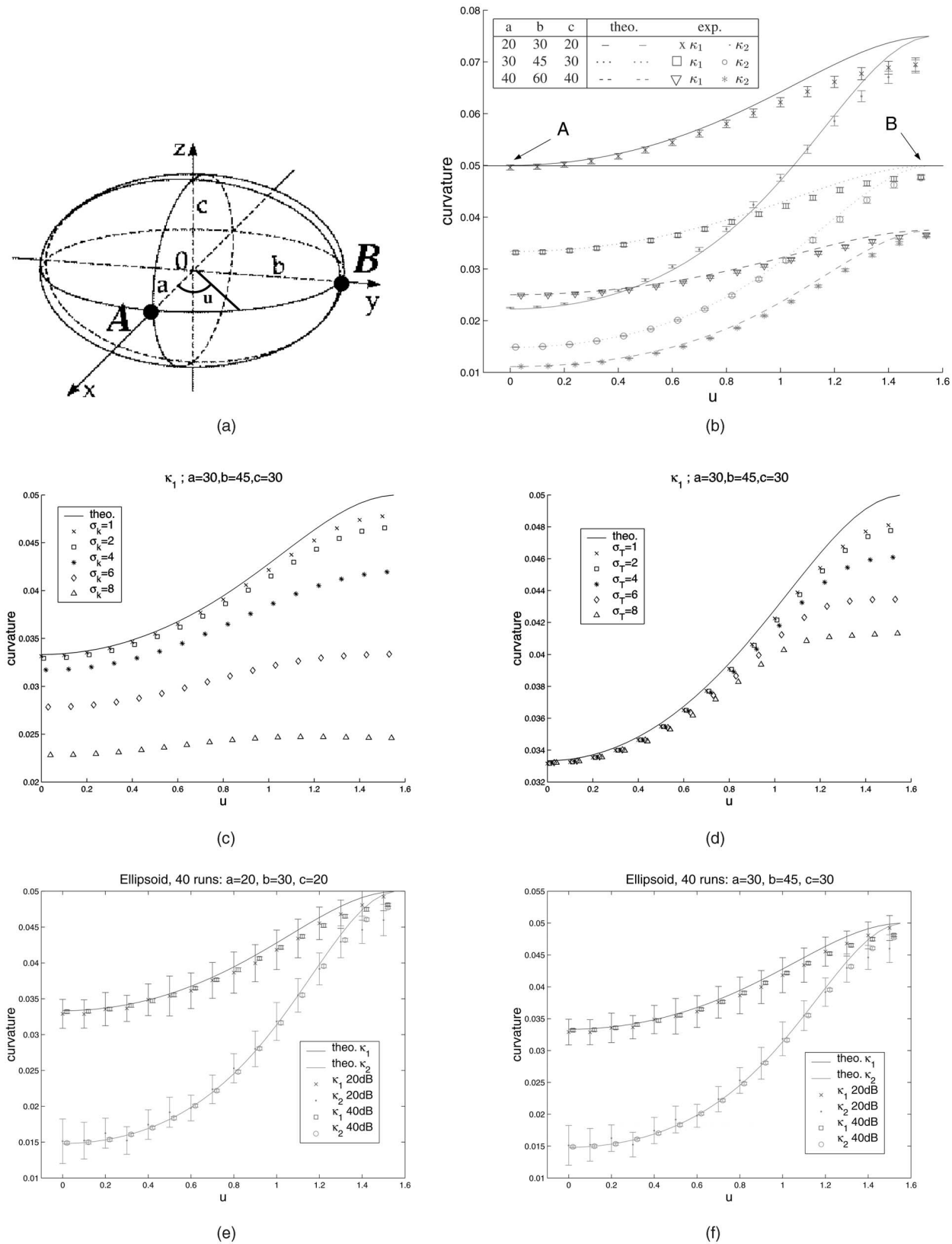


Fig. 1. (a) Ellipsoid with half axes a, b, c . Principal curvatures $\kappa_{1,2}$ in xy -plane as a function of u with $\sigma_g = 1, \sigma_T = 2, \sigma_k = 1$. (b) Three ellipsoid shapes for 20 random positions. (c) Influence of σ_k on κ_1 . (d) Influence of σ_T on κ_1 . (e) and (f) Influence of noise on κ_1 and κ_2 averaged over 40 runs.

for higher curvatures can be understood as follows: The derivatives are implemented as convolutions with Gaussians derivatives at scale σ_k . Recall that the curvatures are computed as the derivative of the (mapped) surface normal in the direction of

the principals ((5)), then the average over a surface neighborhood includes surface normals that are not perpendicular to the direction of the derivation, thus have a smaller component than the normal at the point under consideration. Therefore, the more

the local neighborhood is curved the larger the error. This reasoning is also valid in the Knutsson representation where the derivatives are taken, as the Knutsson mapping preserves the local geometry.

In Fig. 1b, two points (A,B) are indicated that lie on two different ellipsoids with the same curvature $\kappa_1 = 0.05$. In A, the estimation is very good ($\epsilon < 1$ percent), although the local geometry is asymmetric ($\kappa_1 \neq \kappa_2$), whereas, at the umbilic point B (equal curvatures in all directions), we observe a larger error ($\epsilon \approx 4$ percent). The reason is that, at A, $\kappa_1 = \text{const.}$ and κ_2 changes slowly, whereas, at B, $\kappa_1 = \kappa_2$ but both are changing rapidly. Hence, the estimation error is not only dependent on the value of the curvature, it also depends on the change of the curvatures in the neighborhood, i.e., the local geometry.

3.2.1 Influence of the Scale of the Filters: $\sigma_g, \sigma_T, \sigma_k$

There are three Gaussian kernel sizes involved in the computation: First, the derivative kernel σ_g to compute the gradient ∇I ; second, the smoothing kernel σ_T of the GST; and, finally, the derivative kernel σ_k applied to the mapped normal field (5). We do not investigate the dependency on the size of σ_g as the smallest reasonable size, $\sigma_g \approx 1$, gives the best gradient [26] and σ_T is much more effective in noise suppression. The influence of σ_k is shown in Fig. 1c. The relative error in Fig. 1d is much smaller for the same size of σ_T as for σ_k in Fig. 1c. This is due to the fact that curvature is a difference of orientations, biased orientation terms (dependent on σ_T and κ) cancel to a limited degree. The actual choice of the size of σ_T for generic neighborhoods is a trade off between noise suppression and accuracy of orientation estimation.

3.2.2 Performance in the Presence of Noise

We hamper the test images with different levels of Gaussian noise to measure the robustness of the estimator. We use the definition $\text{SNR} = 20 \log \frac{S}{\sigma_n^2}$ with σ_n^2 the variance of the Gaussian noise and S the maximal signal strength. In Figs. 1e and 1f, the results are shown for two different ellipsoids. The error-bars indicate the standard deviation over 40 realizations. The estimation is consistent as the mean stays around the true value and the error-bars intersect the true curvature. With increasing noise level only the error-bars become larger, the mean remains stable. For a discussion on noise robustness for traditional methods, see, for example, [28].

3.3 Bending Energy and Surface Area

The estimation performance is investigated for ellipsoids as a function of scale and deformation. In all experiments, the results of the true, the noise free, and two noise level (20, 40dB) are plotted. The results of the noise runs are averaged over 20 realizations and the noise free results over 20 subpixel shifts. For all computation, we keep the following kernel sizes $\sigma_g = \sigma_k = 1, \sigma_T = 2$ fixed.

3.3.1 Ellipsoids, Scaled, and Deformed

The true surface area and bending energy are integrated numerically from the analytically computed curvatures with MATHEMATICA [29]. The results of our computations are shown in Fig. 2a for a scaled ellipsoid and in Fig. 2b for a deformed one. The deformation of an ellipsoid is done by slowly deforming a sphere ($r = 12$) into a elongated cigar-like object ($a = c = 12, b = 38$); whereas the scaled ellipsoid is blown up from $a = c = 12, b = 18$ to $a = c = 36, b = 54$ with constant ratio $b/a = 1.5$. The area estimation is critical to all other estimations. For the noise free case the estimation is nearly error-free. Even in the presence of noise, the area estimation is fine. The bending energy is a scale invariant property. In Fig. 2a, we see that the curve for the noise free and for 40dB indeed approach a constant value. For 20dB, the curvature estimation for larger ellipsoids seems to be influenced by the noise in a scale variant manner because the area estimation remains fine. As higher curvatures

are more biased (Section 3.2), we expect the estimation to perform better for larger ellipsoids. The quality of the estimation of the bending energy, however, decrease with increasing ratio b/a (elongation). The curvature increases in some areas during deformation such that the bending energy increases. These larger values will contribute to a slightly larger negative bias as explained in Section 3.2.

4 APPLICATION AND COMPARISON WITH EXISTING WORK

We compare our method with the classical Hessian based isophote curvature and a method presented by Thirion and Gourdon [4]. They compute the curvatures directly from the first and second derivatives of the image. For further work on 3D curvature, see, for example, [30], [31], [3], [32], [33]. In the Hessian approach, the Hessian matrix is rotated to be aligned with the surface normal. Then, the surface subspace Hessian is diagonalized and the curvatures are computed as these eigenvalues divided by the gradient magnitude [34], [2].

In Figs. 2c, 2d, 2e, and 2f, we show different vertical slices through a synthetic 3D torus shell and the calculated mean curvatures $H = \frac{1}{2}(\kappa_1^2 + \kappa_2^2)$. In Fig. 2d, the estimation by our algorithm (5) is shown; in Fig. 2e, the numerator of the mean curvature by Thirion et al. [4]; and, in Fig. 2f, the mean curvature by Thirion et al. [4]. Comparing Figs. 2e and 2f, we see that the numerator is smooth, but that at the peak position of the ridge profile the normalization fails as the gradient magnitude is (nearly) zero. These positions display white in Fig. 2f. Note the sign change in Fig. 2e on different sides of the ridge. In a coordinate independent description (arbitrary choice of the origin), the sign of curvature is not meaningful for ridges as the sign cannot be defined consistently from local information only (Appendix A). For edges, this is trivial as by convention the inside of objects is white.

In Figs. 3d, 3e, and 3f, we apply 3D surface curvature estimation to a 3D CT image of a tree trunk. In Fig. 3c, the input image is shown. Our estimator as in (5) computes a smooth curvature field. The isophote approach via the Hessian fails on the ridges (white rings in the input image) and valleys (dark rings). The estimation algorithm of Thirion et al. [4] (12), (13), and (14) does not overcome these problems either. Furthermore, in any application where patterns of ridge-like structures are present a robust estimation is not possible by the isophote curvature. First, on the ridges and valleys the gradient magnitude vanishes which results in a very high overestimation. Second, efficient noise reduction is not possible as it requires large smoothing kernels which smooth out the pattern of interest, such that the signal vanishes. Our algorithm can reliably estimate curvature in these cases.

The reason for these properties is that our algorithm uses a two step approach: First, an orientation estimation process in a local neighborhood described by σ_T and then the derivative of the orientation field yields the curvature. In our algorithm, σ_g, σ_k are the smoothing parameters for the first and second order derivative and correspond to the smoothing parameter of the isophote curvature. For $\sigma_T \rightarrow 0$, the GST returns the input vector as only eigenvector and our proposed method is equal to the isophote curvature. More explicitly, the added value of our estimation algorithm is a robust orientation estimate avoiding gradient magnitude normalization through the use of a local neighborhood σ_T .

5 CONCLUSION

We have demonstrated that our approach to estimate curvature and (local) shape descriptors on surfaces based on the differential structure of images works. It avoids problems associated with classical approaches such as matched filtering and polynomial fitting. It succeeds where isophote curvature fails. Furthermore, we can conclude that the GST is able to estimate the principal

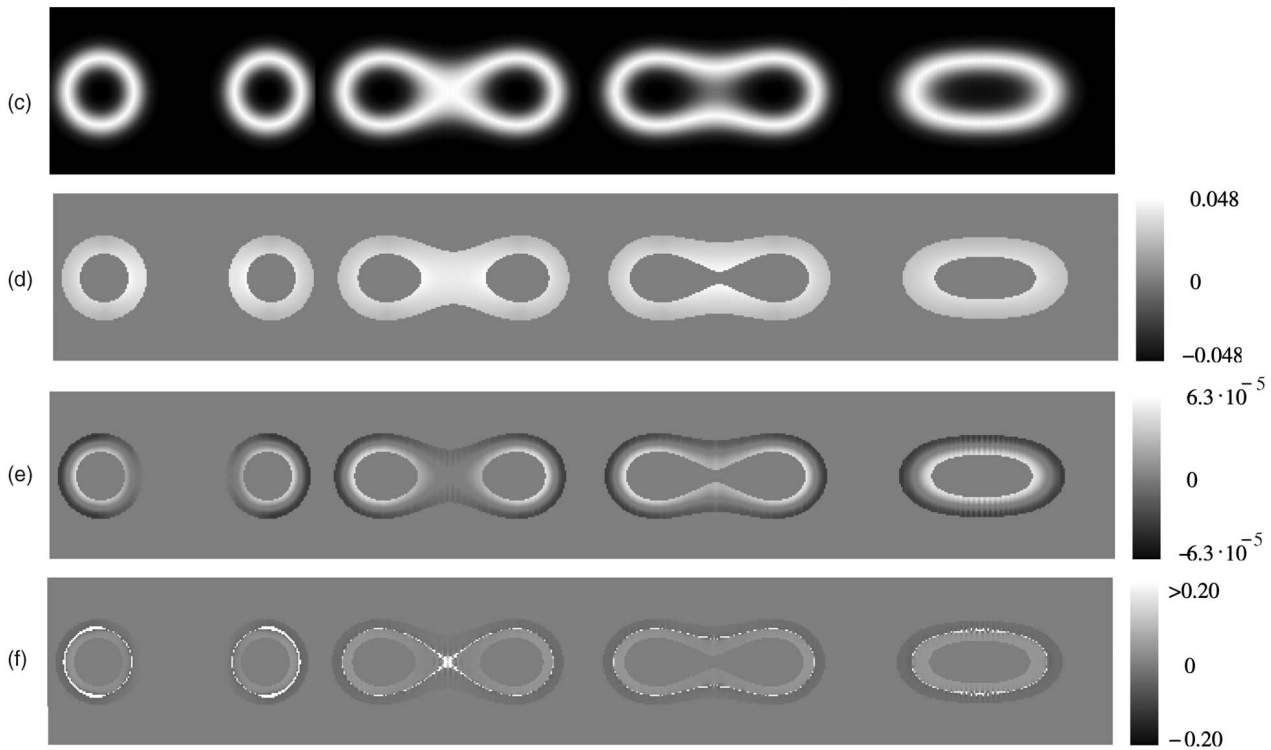
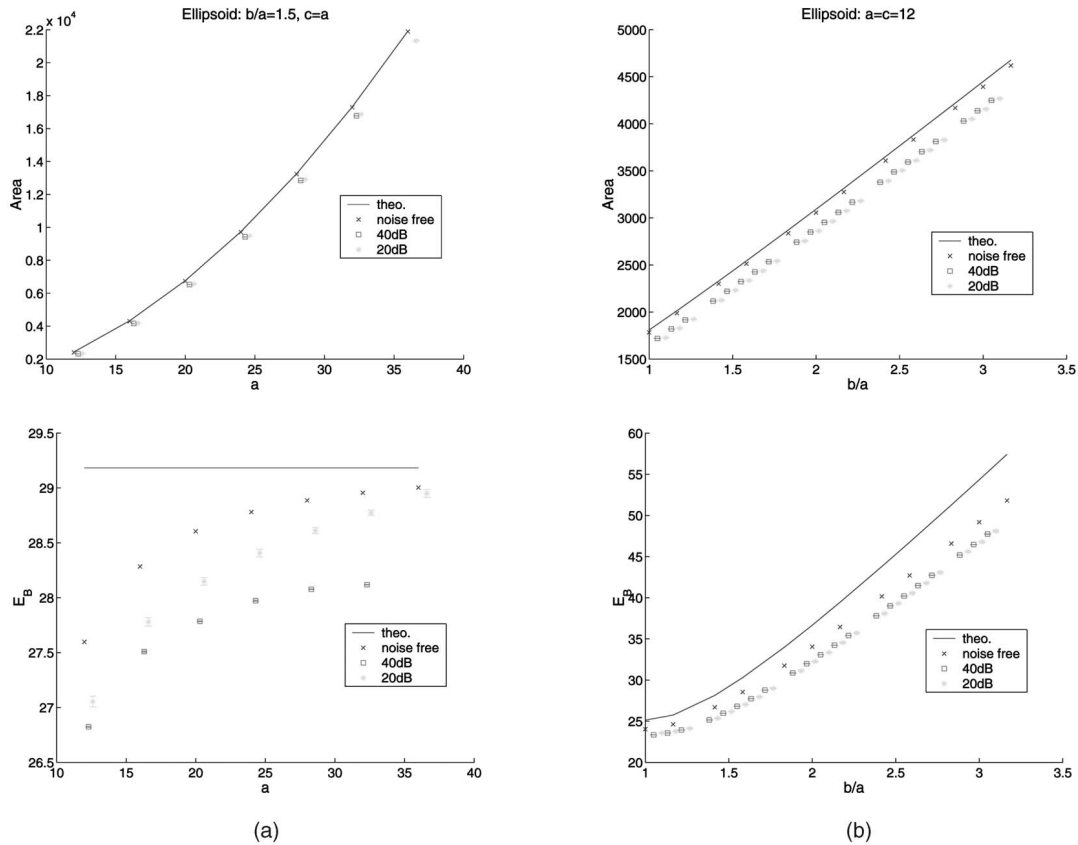


Fig. 2. (a) and (b) Estimates of surface area, bending energy E_B for ellipsoids at different noise levels averaged over 20 runs with $\sigma_g = 1, \sigma_T = 2, \sigma_k = 1$ (a) as a function of a , with fixed ratio $b/a = 1.5, c = a$; (b) as a function of the ratio b/a , with $a = c = 12$; (c) vertical slices through a 3D torus shell with radii $R = 50$ and $r = 15$ and Gaussian ridge profile; (d) mean curvature by (5); $\sigma_g = 1, \sigma_T = 3, \sigma_k = 1$; (e) numerator of the mean curvature by Thirion et al. [4] $\sigma = 1$; (f) mean curvature by Thirion et al. [4].

directions on surfaces, as the computed curvatures in these directions are estimated accurately. Our new curvature estimation formula (5) is a consequence of the formulas of differential geometry taking into account the structure of gray-level images,

e.g., circumventing the problem of nonunique orientation representation by using the Knutsson mapping. The main advantage of our algorithm is that the orientation estimation and the curvature computation are done in two steps in contrary to the isophote

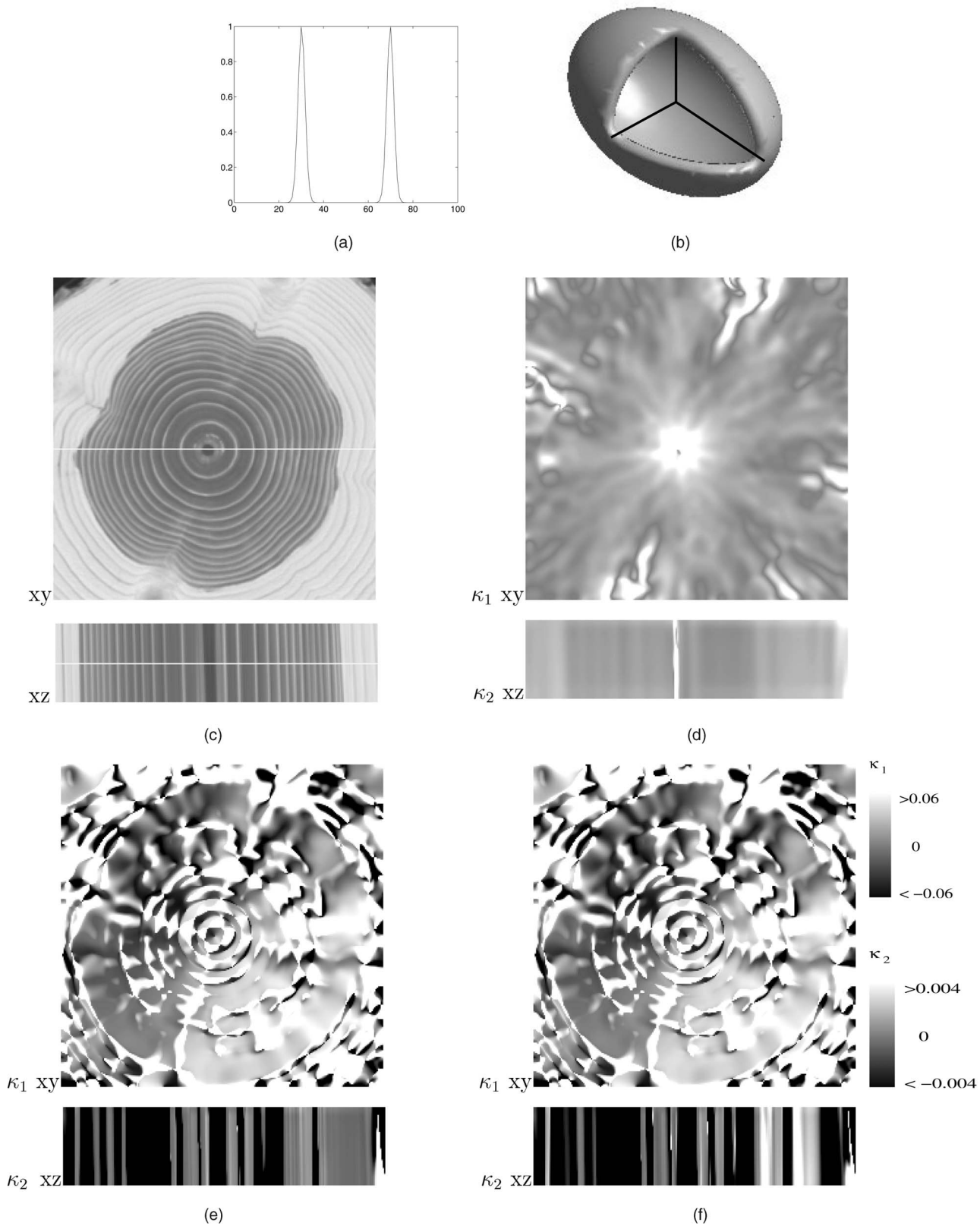


Fig. 3. (a) Cross sections through an ellipsoid shell. (b) An ellipsoid shell where one octant is cut out. (c) Image of a tree trunk (xy and xz cross sections). (d) Estimated principal curvatures by (5), $\sigma_g = 1, \sigma_T = 4$. (e) Principal isophote curvatures via the Hessian at scale $\sigma = 4$. (f) Principal curvatures at scale $\sigma = 4$ according to Thirion et al. [4] (12), (13), and (14). (d), (e), and (f) Display: $\kappa_1: [-.06,.06], \kappa_2: [-.004,.004]$.

approach [4]. Therefore, the local orientation estimation can be done accurately with the GST (which includes the large regularization kernel σ_T for noise suppression) and, from this orientation data, the curvature is computed (small derivative kernel σ_k) by

differential geometry formulation using a closed-form orientation representation. Even for shell-like objects, the sign of curvature can be retrieved. The error of the computed curvature is dependent on the size of the curvature and its change in the local neighborhood.

Nevertheless, the error stays small ($\epsilon < 7$ percent for $\kappa < 0.08$) and the estimation is robust in the presence of noise. Surface area estimation and integration of functions over these embedded surfaces can be performed sampling-error free by relation (6). It performs without bias and is independent of scale and local geometry. From these two ideas, curvature based shape descriptors, the bending energy, and Euler characterization can be computed. The estimation of these descriptors is consistent, robust, and independent of the scale of the objects. There is little relative error for isotropic objects with small curvature ($\epsilon < 0.5$ percent for $\kappa < 0.03$) and for highly asymmetric shapes and high curvatures the error stays small ($\epsilon < 7$ percent for $\kappa < 0.08$).

APPENDIX A

SOLID OBJECTS FROM SHELLS AND THE SIGN OF CURVATURE

Reconstructing a solid object from a shell is achieved by preliminary filling the shell by the gray-weighted distance transform [35], [36]. Now, we can distinguish interior from exterior parts of the object. This yields a sign which we can add to the estimated orientation field and obtain the normal vector field. Together with the original object shells in the input image, we can create a gradient vector image from which we can obtain solid objects by an advanced integration technique [37]. The sign of the surface principal curvatures for shell like object in gray-value images is obtained by investigating the value of the second derivative along the tangent direction T^iHT , where H is the Hessian matrix of the image, so a maximum/minimum corresponds to a negative/positive value.

APPENDIX B

PROOF OF (5)

Equation 2 reads in index notation (with summation over same indices) $\kappa^2 = \sum_i [T^i \partial_i N_i]^2$. With relations (3), a normalized normal $\sum_i N_i^2 = 1$ and the mapping $M(N) = N_i N_k$, (5) reads

$$2\kappa^2 = \sum_{l,k} [T^i \partial_i N_l N_k]^2 = \sum_{l,k} N_l^2 (T^i \partial_i N_k)^2 + N_k^2 (T^i \partial_i N_l)^2 + 2N_l N_k (T^i \partial_i N_k)(T^i \partial_i N_l) \quad (7)$$

$$= \sum_l N_l^2 \sum_k (T^i \partial_i N_k)^2 + \sum_k N_k^2 \sum_l (T^i \partial_i N_l)^2 + 2 \sum_l N_l (T^i \partial_i N_l) \sum_k N_k (T^i \partial_i N_k) \quad (8)$$

$$= 2 \sum_l [T^i \partial_i N_l]^2 + 2 \left[\sum_l N_l (T^i \partial_i N_l) \right]^2 = 2 \sum_l [T^i \partial_i N_l]^2 + 2 \left[\sum_l T^i \partial_i \frac{1}{2} N_l^2 \right]^2 = 2 \sum_l [T^i \partial_i N_l]^2. \quad (9)$$

ACKNOWLEDGMENTS

This work was partially supported by the Netherlands Organization for Scientific Research NWO, grant number 612-012-003.

REFERENCES

- [1] P.W. Verbeek, "A Class of Sampling-Error Free Measures in Oversampled Band-Limited Images," *Pattern Recognition Letters*, vol. 3, pp. 287-292, 1985.
- [2] L.J. van Vliet and P.W. Verbeek, "Curvature and Bending Energy in Digitized 2D and 3D Images," *Proc. Eighth Scandinavian Conf. Image Analysis*, pp. 1403-1410, 1993.
- [3] B.M. ter Haar Romeny, L.M.J. Florack, A.H. Salden, and M.A. Viergever, "Higher Order Differential Structure of Images," *Image and Vision Computing*, vol. 12, no. 6, pp. 317-325, 1994.
- [4] J.P. Thirion and A. Gourdon, "Computing the Differential Characteristics of Isointensity Surfaces," *Computer Vision and Image Understanding*, vol. 61, no. 2, pp. 190-202, 1995.

- [5] P. Breton and S.W. Zucker, "Shadows and Shading Flow Fields," *Proc. IEEE Conf. Computer Vision and Pattern Recognition (CVPR '96)*, pp. 782-789, 1996.
- [6] J.B.A. Maintz, P.A. van den Elsen, and M.A. Viergever, "Evaluation of Ridge Seeking Operators for Multimodality Medical Image Matching," *IEEE Trans. Pattern Analysis and Machine Intelligence*, vol. 18, no. 4, pp. 353-365, 1996.
- [7] J. van de Weijer, L.J. van Vliet, P.W. Verbeek, and M. van Ginkel, "Curvature Estimation in Oriented Patterns Using Curvilinear Models Applied to Gradient Vector Fields," *IEEE Trans. Pattern Analysis and Machine Intelligence*, vol. 23, no. 9, pp. 1035-1042, Sept. 2001.
- [8] H. Knutsson, "Producing a Continuous and Distance Preserving 5-D Vector Representation of 3-D Orientation," *Proc. IEEE Computer Soc. Workshop Computer Architecture for Pattern Analysis and Image Database Management*, pp. 175-182, Nov. 1985.
- [9] H. Knutsson, "Representing Local Structure Using Tensors," *Proc. Sixth Scandinavian Conf. Image Analysis*, pp. 244-251, June 1989.
- [10] B. Rieger and L.J. van Vliet, "Representing Orientation in N-Dimensional Spaces," *Proc. 10th Int'l Conf. Computer Analysis of Images and Patterns*, N. Petkov and M.A. Westenberg, eds., Aug. 2003.
- [11] J.S. Duncan, F.A. Lee, A.W.M. Smeulders, and B.L. Zaret, "A Bending Energy Model for Measurement of Cardiac Shape Deformity," *IEEE Trans. Medical Imaging*, vol. 10, no. 3, pp. 307-319, 1991.
- [12] I.T. Young, J.E. Walker, and J.E. Bowie, "An Analysis Technique for Biological Shape I," *Information and Control*, vol. 25, no. 4, pp. 357-370, Aug. 1974.
- [13] J. Serra, *Image Analysis and Mathematical Morphology*. Academic Press, 1982.
- [14] R. van den Boomgaard, "Affine Invariant Deformation Curves a Tool for Shape Characterization," *Image and Vision Computing*, vol. 17, pp. 375-380, 1999.
- [15] C.L. Luengo Hendriks and L.J. van Vliet, "A Rotation-Invariant Morphology for Shape Analysis of Anisotropic Objects and Structures," *Proc. Fourth Int'l Workshop Visual Form*, C. Arcelli, L.P. Cordella, and G. di Baja Sanniti, eds., 2001.
- [16] T. Frankel, *The Geometry of Physics*. Cambridge Univ. Press, 1997.
- [17] M.P. do Carmo, *Differential Geometry of Curves and Surfaces*. Prentice Hall, 1976.
- [18] J.J. Koenderink and A.J. van Doorn, "Surface Shape and Curvature Scales," *Image and Vision Computing*, vol. 10, no. 8, pp. 557-565, 1992.
- [19] H. Knutsson, "Filtering and Reconstruction in Image Processing," PhD thesis, Linköping Univ., Linköping, Sweden, 1982.
- [20] M. Kass and A. Witkin, "Analyzing Oriented Patterns," *Computer Vision, Graphics, and Image Processing*, vol. 37, pp. 362-385, 1987.
- [21] B. Jähne, *Digital Image Processing*, fourth ed. Springer, 1997.
- [22] S. di Zenò, "A Note on the Gradient of a Multi-Image," *Computer Vision, Graphics, and Image Processing*, vol. 33, pp. 166-125, 1986.
- [23] J. Bigün, G.H. Granlund, and J. Wiklund, "Multidimensional Orientation Estimation with Applications to Texture Analysis and Optical Flow," *IEEE Trans. Pattern Analysis and Machine Intelligence*, vol. 13, no. 8, pp. 775-790, Aug. 1991.
- [24] R. van den Boomgaard and J. van de Weijer, "Robust Estimation of Orientation for Texture Analysis," *Proc. the Second Int'l Workshop Texture Analysis and Synthesis*, pp. 135-138, June 2002.
- [25] P.W. Verbeek and L.J. van Vliet, "Estimators of 2D Edge Length and Position, 3D Surface Area and Position in Sampled Gray-Valued Images," *Biomed. Eng. Online*, vol. 1, no. 1, pp. 46-61, 1993.
- [26] P.W. Verbeek and L.J. van Vliet, "On the Location Error of Curved Edges in Low-Pass Filtered 2-D and 3-D Images," *IEEE Trans. Pattern Analysis and Machine Intelligence*, vol. 16, no. 7, pp. 726-733, July 1994.
- [27] J. Weickert, B.M. ter Haar Romeny, and M.A. Viergever, "Efficient and Reliable Schemes for Nonlinear Diffusion Filtering," *IEEE Trans. Image Processing*, vol. 7, no. 3, pp. 398-410, 1998.
- [28] A. Hilton, J. Illingworth, and T. Windeatt, "Statistics of Surface Curvature Estimates," *Pattern Recognition*, vol. 28, no. 8, pp. 1201-1221, 1995.
- [29] Wolfram Research, "Mathematica 4," www.wolfram.com, 1998.
- [30] P. Parent and S.W. Zucker, "Trace Inference, Curvature Consistency, and Curve Detection," *IEEE Trans. Pattern Recognition and Machine Intelligence*, vol. 11, no. 8, pp. 823-839, Aug. 1989.
- [31] O. Monga, N. Ayache, and P.T. Sander, "From Voxel to Intrinsic Surface Features," *Image and Vision Computing*, vol. 10, no. 6, pp. 403-417, 1992.
- [32] L.A. Iverson and S.W. Zucker, "Logical/Linear Operators for Image Curves," *IEEE Trans. Pattern Analysis and Machine Intelligence*, vol. 17, no. 10, pp. 982-996, Oct. 1995.
- [33] A.H. Salden, B.M. ter Haar Romeny, and M.A. Viergever, "Differential Integral Geometry of Linear Scale-Space," *J. Math. Imaging and Vision*, vol. 9, pp. 5-27, 1998.
- [34] H. Bärman, G.H. Granlund, and H. Knutsson, "Estimation of Curvature in 3-D Images Using Tensor Field Filtering," *Proc. Conf. Computer Vision*, O. Faugeras, ed., pp. 563-565, 1990.
- [35] D. Rutovitz, "Datastructures for Operations on Digital Images," *Pictorial Pattern Recognition*, G.C. Cheng, R.S. Ledley, D.K. Pollock, and A. Rosenfeld, eds., pp. 105-133, 1968.
- [36] P.W. Verbeek and B.J.H. Verwer, "Shading from Shape, the Eikonal Equation Solved by Gray-Weighted Distance Transform," *Pattern Recognition Letters*, vol. 11, pp. 681-690, 1990.
- [37] P.W. Verbeek and J. Dijk, "The D-Dimensional Inverse Vector-Gradient Operator and Its Application for Scale Free Image Enhancement," *Proc. 10th Int'l Conf. Computer Analysis of Images and Patterns*, N. Petkov and M.A. Westenberg, eds., Aug. 2003.